

ENERGY DISSIPATION PRESERVING PHYSICS INFORMED NEURAL NETWORK FOR ALLEN-CAHN EQUATIONS

A PREPRINT

✉ **Mustafa Kütük**

Institute of Applied Mathematics
Middle East Technical University
06800, Ankara, Türkiye
mkutuk@metu.edu.tr

✉ **Hamdullah Yücel**

Institute of Applied Mathematics
Middle East Technical University
06800, Ankara, Türkiye
yuclh@metu.edu.tr

March 14, 2025

ABSTRACT

This paper investigates a numerical solution of Allen–Cahn equation with constant and degenerate mobility, with polynomial and logarithmic energy functionals, with deterministic and random initial functions, and with advective term in one, two, and three spatial dimensions, based on the physics-informed neural network (PINN). To improve the learning capacity of the PINN, we incorporate the energy dissipation property of the Allen-Cahn equation as a penalty term into the loss function of the network. To facilitate the learning process of random initials, we employ a continuous analogue of the initial random condition by utilizing the Fourier series expansion. Adaptive methods from traditional numerical analysis are also integrated to enhance the effectiveness of the proposed PINN. Numerical results indicate a consistent decrease in the discrete energy, while also revealing phenomena such as phase separation and metastability.

Keywords Phase fields models · Allen–Cahn equation · Physics informed neural network · Energy dissipation

1 Introduction

Phase field models have a central role to understand the behaviour of the many complicated moving interface problems in material science [1], fluid dynamics [2], fracture mechanics [3, 4], image analysis [5], and mean curvature flow [6]. Among these models, Allen-Cahn introduced in [7] to describe the motion of anti-phase boundaries in crystalline solids at a fixed temperature is a particular case of gradient flows in the form of

$$u_t = -\mu(u) \frac{\delta \mathcal{E}(u)}{\delta u}, \quad (1)$$

where $\frac{\delta \mathcal{E}(u)}{\delta u}$ represents the variational derivative of the free energy taken in the $L^2(\Omega)$ -norm with $\Omega \subset \mathbb{R}^d$ ($d = 1, 2, 3$) as follows

$$\mathcal{E}(u) = \int_{\Omega} \left(\frac{\epsilon^2}{2} |\nabla u|^2 + F(u) \right) d\mathbf{x}. \quad (2)$$

Specifically, the Allen-Cahn equation corresponds to a nonlinear partial differential equation (PDE) in the form of

$$u_t = \mu(u)(\epsilon^2 \Delta u - f(u)), \quad (\mathbf{x}, t) \in \Omega \times (0, T], \quad (3)$$

with the initial condition

$$u(\mathbf{x}, t = 0) = u_0(\mathbf{x}) \quad \mathbf{x} \in \Omega,$$

and appropriate boundary conditions such as the Dirichlet, Neumann, or periodic boundary condition. Here, u denotes the concentration of one the species of the alloy, known as the phase state between materials, on a bounded domain $\Omega \subset \mathbb{R}^d$ ($d = 1, 2, 3$) with the Lipschitz boundary $\partial\Omega$, ϵ represents the small interfacial length during the phase

separation process, and $\mu(u)$ is the non-negative mobility function. Moreover, the nonlinear $f(u)$ is the derivative of a free energy functional $F(u)$, which is characterized by logarithmic or polynomial functions. The logarithmic free energy potential (see, e.g., [8]) can be formulated as

$$F(u) = \frac{\theta}{2}[(1+u)\ln(1+u) + (1-u)\ln(1-u)] - \frac{\theta_c}{2}u^2, \quad 0 < \theta \leq \theta_c, \quad (4)$$

where θ and θ_c are absolute and transition temperatures, respectively. The derivative of the logarithmic free energy potential is then equivalent to

$$f(u) = F'(u) = \frac{\theta}{2} \ln \left[\frac{1+u}{1-u} \right] - \theta_c u.$$

On the other hand, the polynomial free energy potential, also called as quartic double-well, is an approximation of the logarithmic ones when the temperature θ closes to θ_c , formulated as follows

$$F(u) = \frac{1}{4}(1-u^2)^2, \quad (5)$$

and its derivative is $f(u) = u^3 - u$. It is well-known that the solution $u(\mathbf{x}, t)$ of the Allen-Cahn equation has two crucial properties; the decay of the total free energy for $\mu(u) > 0$, that is,

$$\frac{d\mathcal{E}(u(t))}{dt} \leq 0, \quad (6)$$

which is a typical property of the gradient flows, and the maximum bound principle. In the double-well potential (5), the solution always stays inside the interval $[-1, 1]$, while the solution of the logarithmic potential (4) is bounded in the interval $[-s, s]$ for all the time, where $1 > s > 0$ is the constant satisfying $f(s) = 0$.

The Allen-Cahn equation (3) has been the subject of a great deal of research, primarily because of its relationship with intriguing and complex geometric problems involving moving surfaces; see, e.g. [9, 10, 11] and references therein. As ϵ tends towards zero, the solution of the Allen-Cahn equation (3) behaves like a piecewise constant with values ± 1 , in much of two bulk regions which are separated by a diffusive interfacial layer of thickness $\mathcal{O}(\epsilon)$. For finite but small ϵ , the solution within this interfacial layer remains smooth but it develops a large spatial gradient. Such layers move in time, mimicking dynamically evolving fronts. Because of that, the Allen-Cahn equation has been considered as one of the fundamental model equations for the diffuse interface approach developed to study phase transitions and interfacial dynamics in materials science [12]. In [7], it was first formally proved that the zero level set of the solution u converges to a surface denoted by Γ_t which evolves according to the geometric law $V = \kappa$, where V represents the normal velocity of the surface Γ_t and κ is its mean curvature. Later, Evans et al. in [13] rigorously justified this limit by proving a comprehensive result: for $t \geq 0$, the limit of the zero level set of the solution u is encompassed within the generalized solution of the motion by mean curvature flow, as established in [14, 15]. Then, it was also shown in [16] that this limit is one of Brakke's motion by mean curvature solution.

Clearly, the Allen-Cahn equation (3) is crucial for understanding phase transitions in materials science and examining curvature-driven flows in geometry. It is especially valuable when singularities arise in these flows, as the solution u persists over time, requiring minimal adjustments to manage potential singularities. While analytical methods are used to understand the dynamics of the solutions, explicit analytic solutions are generally not possible due to the nonlinearity of the equation. Therefore, it becomes essential to find an efficient and accurate numerical solution. However, it is not an easy task due to the existence of a nonlinear term and of the small interfacial length parameter ϵ . An extensive numerical investigation of the Allen-Cahn equations has been studied by using different numerical techniques in the spatial domain, such as finite element methods in [17], discontinuous Galerkin methods in [18, 19], and in the temporal domain, such as the implicit-explicit (IMEX) techniques [20, 21], the average vector field (AVF) method [19, 22], and the splitting methods [23]. In addition to the discretization approaches, analytical approximate techniques have been used to solve such kind of nonlinear PDEs, such as Adomian decomposition method, homotopy perturbation method, homotopy analysis method, tanh-function method, (variational iteration) method; see, e.g., [24, 25]. In these studies, the primary goal is to find a numerical scheme that satisfies the energy dissipative property (6) and adheres to the maximum bound principle, in addition to obtaining (optimal) a priori error estimates.

The aforementioned numerical methods can be accurate up to the given threshold but they have some restrictions such as mesh dependence, high computational burden for the nonlinear PDEs. On the other hand, in recent years, the usage of deep neural networks (DNNs) has lead to a significant achievement in the several areas, such as visual recognition [26], cognitive science [27] as well as solving differential equations [28, 29, 30, 31, 32, 33, 34]. Among them, Physics-Informed Neural Network (PINN) introduced by Raissi et al. in [32] has received great attention thanks to its flexibility in tackling a wide range of forward and inverse problems involving PDEs. The idea behind PINN is based

on the universal approximation theorem [35, 36], which asserts that a neural network can approximate any function given sufficient complexity. In this structure, weights and biases of the neural network model are optimized according to the loss function, containing the physics of the underlying problem, which are basically governing equations, boundary conditions, and initial condition. Up to now, the PINN has been used to solve different types of problems in computational science and engineering, such as inverse problems [37], fluid dynamics [38, 39], parameter estimation [40], topology optimization [41], fractional PDEs [42], and stochastic PDEs [43, 44]. In addition, different variants of the standard PINN have been proposed to increase the performance of PINN, such as meta-learning [45], gradient-enhanced [46], balance of weights [47], decomposition of spatial domain [48], adaptive sampling [49], adaptivity in temporal domain [50, 51], adaptive activation function [52], and enforcing boundary conditions [53]. Although the PINN has been widely employed for approximating PDEs, theoretical investigations into their convergence and error analysis remain limited. In [54], the authors explain why the PINN works and shows its consistency for the linear elliptic and parabolic PDEs. An estimation of the generalization error by means of the training error and the number of training data points is provided in [55, 56] for forward PDEs and inverse problems. Total error is bounded in terms of training samples, depth and width of the deep neural networks in various studies: [57] for Navier-Stokes equation, [58] for the linear elliptic and parabolic PDEs, [59] for phase field problems, and [60] for hyperbolic PDEs. The mathematical foundation for PINNs in approximating PDE solutions continues to be an active area of research. However, a theoretical discussion is not the scope of the present study and can be considered as a future study. Instead, we mainly focus on presenting a novel PINN framework to solve a class of Allen-Cahn equations. Compared to the conventional methods, such as finite difference, finite element, deep learning approaches like PINN is mesh-free thanks to the automatic differentiation and can avoid the curse of dimensionality; see, e.g., [61]. However, for low dimensional PDEs, it is still not straightforward to claim that the computational accuracy obtained from DNNs is better than the ones obtained by the conventional methods; see, e.g., [62] for more discussion.

Although the standard PINN (std-PINN) has been widely accepted and has yielded remarkable results across a range of problems in the computational science and engineering, it is not always capable of solving the Allen-Cahn equation, a typical example of phase field models, due to the sharp transition layers, evolution of the layers in time, high sensitivity to the initial conditions, or the choice of hyperparameters, including the learning rate, activation function, optimizer, loss function weights, and the width and depth of the neural network. To enhance the efficiency of PINN in solving Allen-Cahn type PDEs, the authors in [63] use two specially designed convolutional neural networks (CNNs) and the loss functions correspond to the full-discrete systems obtained from finite difference methods in both space and time. Similarly, the multi-step discrete time models with adaptive collocation strategy are considered in [64]. The authors in [50] involve the idea of adaptivity in both time and space by sampling the data points, while in [65], the same neural network is retrained over successive time segments, while satisfying the obtained solution for all previous time segments. In addition, the system of the Allen-Cahn equation (3) first reduced into a first-order problem and then the converted minimization problem is approximated by using a deep learning approach in [66]. A theoretical perspective for the propagation of PINN errors is also given in [59] for the Allen-Cahn equations. A recent study by Guo et al. in [67] introduces an adaptive energy-based sequential training method for the PINN approach to enhance their performance in solving the Allen-Cahn equation, particularly for long-duration simulations. In the aforementioned works, the proposed PINN structures are usually tested on the Allen-Cahn equations with polynomial potentials, while to the best of our knowledge there is no PINN work on the Allen-Cahn equations with logarithmic potentials, where the nonlinearity plays a more critical role. In addition, the behavior of the energy functional, which is physically more crucial for such kind of problems, is often neglected. Contrary to the previous studies, we here propose a novel methodology based on preserving of the energy dissipation to predict the dynamics of the Allen-Cahn equation with constant and degenerate mobility, with polynomial and logarithmic energy functionals, with deterministic and random initial functions, and with advective term in one, two, and three spatial dimensions. The proposed network approach guarantees the decay of energy and also plays a key role in accurately learning the dynamics of the Allen-Cahn equation. Embedding of different conservation constraints, such as mass and momentum conservation, into the PINN architecture are also considered in [68, 69] for different types of PDEs.

Our specific contributions can be summarized as:

- We propose a novel PINN approach based on preserving of the energy dissipation to learn the dynamics of the Allen-Cahn equation more accurately.
- We offer a detailed set of benchmark examples to evaluate the performance of the proposed approach. These examples include logarithmic and polynomial free energy potentials, constant and degenerate mobility functions, deterministic and random initial functions, and advective term in one, two, and three spatial dimensions.

The rest of this manuscript is outlined as follows: In next section, we briefly review the standard physics-informed neural network (std-PINN). In Section 3, we introduce our main contribution, which is the addition of energy dissipation

constraint (6) into the loss function. Section 4 presents numerical strategies utilizing adaptive approaches to enhance the performance of the PINN. Numerical simulations of various benchmark problems are provided in Section 5. Last, we give some concluding remarks in Section 6 based on the findings in the paper.

2 Physics-informed neural network

In this section, we first review the nonlinear mapping in the deep learning architecture [70], and then the standard physics-informed neural network (std-PINN) introduced in [32].

Let a neural network of depth L , that is, $\mathcal{N}^L(\mathbf{x}) : \mathbb{R}^{N_0} \rightarrow \mathbb{R}^{N_L}$ consist of one input layer, $L - 1$ hidden layer, and one output layer. Each layer which contains N_ℓ neurons transmits the output \mathbf{x}^ℓ to the $(\ell + 1)$ th layer as the input data. The connection between layers is constructed by an affine transformation \mathcal{T} and an activation function $\sigma(\cdot)$

$$\mathbf{x}^\ell = \sigma(\mathcal{T}_\ell(\mathbf{x}^{\ell-1})) = \sigma(w^{\ell-1}\mathbf{x}^{\ell-1} + b^{\ell-1}),$$

where $w^{\ell-1} \in \mathbb{R}^{N_\ell \times N_{\ell-1}}$ and $b^{\ell-1} \in \mathbb{R}^{N_\ell}$ denote the weight and bias of the ℓ th layer, respectively. In general, linear functions are often inadequate for capturing the complexity of a problem. Therefore, nonlinear functions such as ReLU, sigmoid, tanh, swish, etc. [71] are commonly used as activation functions. Hence, for a given input \mathbf{x}^0 , we have

$$\hat{u}(\mathbf{x}^0, \theta) = (\sigma \circ \mathcal{T}_L \circ \sigma \circ \mathcal{T}_{L-1} \circ \cdots \circ \sigma \circ \mathcal{T}_1)(\mathbf{x}^0),$$

where $\hat{u}(\cdot, \cdot)$ is the output of the learning process and $\theta = \{w^\ell, b^\ell\}_{\ell=1}^L$ represent the trainable parameters. Typically, the same activation function is applied to all hidden layers. However, the activation function of the output layer can differ from those of the hidden layers, depending on the structure of the problem. Before training a neural network, θ is need to be initialized by for instance, Xavier initialization [72], He initialization [73], etc.

Let $\Omega \subset \mathbb{R}^d$ ($d = 1, 2, 3$) be an open bounded domain in \mathbb{R}^d with a sufficiently smooth boundary $\partial\Omega$, and $(0, T]$ be a time interval with $T < +\infty$. Then, a general form of a m th order partial differential equation is given in the form of

$$u_t + \mathcal{N}(u, u_{\mathbf{x}}^{(1)}, u_{\mathbf{x}}^{(2)}, \dots, u_{\mathbf{x}}^{(m)}) = 0 \quad \mathbf{x} \in \Omega \subset \mathbb{R}^d, t \in (0, T], \quad (7)$$

where \mathbf{x} and t denote the spatial component with $\Omega \subset \mathbb{R}^d$ and time, respectively. $\mathcal{N}(\cdot)$ is a nonlinear function of the solution $u(\mathbf{x}, t)$ and its spatial derivatives $(u_{\mathbf{x}}^{(1)}(\mathbf{x}, t), u_{\mathbf{x}}^{(2)}(\mathbf{x}, t), \dots, u_{\mathbf{x}}^{(m)}(\mathbf{x}, t))$. Corresponding boundary and initial conditions are given, respectively, by

$$\mathcal{B}(u, u_{\mathbf{x}}^{(1)}, \dots, u_{\mathbf{x}}^{(m-1)}) = G(\mathbf{x}, t) \quad (\mathbf{x}, t) \in \partial\Omega \times (0, T], \quad (8)$$

$$u(\mathbf{x}, 0) = H(\mathbf{x}) \quad \mathbf{x} \in \Omega, \quad (9)$$

where the operator $\mathcal{B}(\cdot)$ allows Dirichlet, Neumann, periodic, and also higher order boundary conditions. Our aim is to develop a numerical solution for the PDE problem (7) with the boundary condition (8) and the initial condition (9) using the neural networks.

In the prediction process of std-PINN, the spatial and temporal points constitute the inputs of network and randomly initialized parameters are updated by minimizing the loss function in the PINN formulation, including three error components defined on the residual, initial condition, and boundary conditions in the sense of the mean-squared error (MSE). Denoting $\hat{u}(\mathbf{x}, t)$ as the output of neural network, the components of the total loss function are introduced as follow:

- MSE on the residual PDE

$$\text{loss}_r = \frac{1}{n_r} \sum_{k=1}^{n_r} \left(\underbrace{\hat{u}_t(\mathbf{x}_k^r, t_k^r) + \mathcal{N}(\hat{u}(\mathbf{x}_k^r, t_k^r), \dots, \hat{u}_{\mathbf{x}}^{(m)}(\mathbf{x}_k^r, t_k^r))}_{R(\mathbf{x}_k^r, t_k^r)} \right)^2, \quad (10)$$

where $(\mathbf{x}_k^r, t_k^r) \in \Omega \times (0, T]$ and n_r denote the interior collocation points and its size, respectively.

- MSE on the initial condition

$$\text{loss}_i = \frac{1}{n_i} \sum_{k=1}^{n_i} \left(\underbrace{\hat{u}(\mathbf{x}_k^i, 0) - H(\mathbf{x}_k^i)}_{I(\mathbf{x}_k^i)} \right)^2, \quad (11)$$

where n_i is the number of initial training data $\mathbf{x}_k^i \in \Omega$.

- MSE on the boundary conditions

$$\text{loss}_b = \frac{1}{n_b} \sum_{k=1}^{n_b} \left(\underbrace{\mathcal{B}(\hat{u}(\mathbf{x}_k^b, t_k^b), \dots, \hat{u}_x^{(m-1)}(\mathbf{x}_k^b, t_k^b)) - G(\mathbf{x}_k^b, t_k^b)}_{B(\mathbf{x}_k^b, t_k^b)} \right)^2, \quad (12)$$

where $(\mathbf{x}_k^b, t_k^b) \in \partial\Omega \times (0, T]$ represents the set of training points to compute MSE on the boundary for various times and n_b is the number of training points on the boundary.

In the PINN structure, the derivatives of the network with respect to time t and space \mathbf{x} are computed by the automatic differentiation [74]. On the other hand, the choice of sampling strategy of collocation points (\mathbf{x}_k, t_k) in the training of PINNs is crucial for enhancing both the accuracy and computational efficiency. Typically, in many PINN studies, the collocation points are determined at the start of the training and remain unchanged throughout the process. In this context, equispaced uniform grids and uniformly random sampling are two basic sampling methods. However, there are also other techniques, such as Latin hypercube sampling (LHS) [75] and Sobol sampling [76]. The LHS is a stratified Monte Carlo sampling technique that produces random samples distributed within intervals, ensuring equal probability and a normal distribution for each range. In contrast, the Sobol sequence, a type of quasirandom low-discrepancy sequence, is often utilized as an alternative to uniformly distributed random numbers and typically yield superior results in various applications, including numerical integration. Instead of utilizing fixed residual points throughout the training process, one could opt to select a new set of residual points at every specified optimization iteration; see, e.g., [31]. Further, recent studies, such as [31, 50, 77] have shown that adaptive sampling strategies significantly enhance the distribution of residual points during training, leading to improved accuracy; see Section 4 for a detailed discussion.

Hence, the total loss function of the std-PINN is given by adding all the aforementioned mean-square errors

$$\text{Loss}(\theta) = \lambda_r \text{loss}_r(\theta) + \lambda_i \text{loss}_i(\theta) + \lambda_b \text{loss}_b(\theta), \quad (13)$$

where θ is the set of trainable parameters, consisting of the weights and biases, and the parameters λ_r , λ_i , and λ_b scale the loss terms. Then, one wishes to find the optimal value of training parameters θ by minimizing the loss function (13) until a given threshold tolerance value or a prescribed maximum number of iterations. In the literature, there are several effective optimization techniques, such as stochastic gradient descent (SGD), L-BFGS, ADAM, etc., see, e.g., [78] and references therein for more details.

3 Penalization of the energy dissipation

To achieve an accurate and efficient numerical approximation for the solutions of nonlinear PDEs, it is essential to maintain the qualitative structures of the underlying system, such as mass conservation and energy dissipation. Motivated by this, we propose a new methodology that focuses on preserving energy dissipation to predict the dynamics of the Allen-Cahn equation.

By following the penalization of the inequality constraints in the optimization theory [79, Chapter 17], we enforce the energy constraint (6) to the loss function (13) weakly by adding the following penalty term

$$\text{loss}_e = \frac{1}{n_e} \sum_{k=1}^{n_e} \left(\max \left(0, \frac{\partial \mathcal{E}}{\partial t} (\hat{u}(\mathbf{x}_k^e, t_k^e)) \right) \right)^2. \quad (14)$$

Here, the energy functional approximation, denoted by $\mathcal{E}(\hat{u})$, is obtained by evaluating the approximated solution \hat{u} at the collocation points (\mathbf{x}_k^e, t_k^e) , whereas the derivative of the energy term with respect to time t is obtained by using automatic differentiation as the previous computations. Finally, our total loss function becomes

$$\text{Loss}(\theta) = \lambda_r \text{loss}_r(\theta) + \lambda_i \text{loss}_i(\theta) + \lambda_b \text{loss}_b(\theta) + \lambda_e \text{loss}_e(\theta), \quad (15)$$

where λ_r , λ_i , λ_b , and λ_e are the scale parameters of the domain residual, initial condition, boundary condition, and energy losses, respectively. Figure 1 illustrates the framework of the proposed PINN approach to solve the Allen-Cahn equation.

4 Adaptive approaches

Now we provide some strategies based on adaptive approaches in the classical numerical techniques to enhance the performance of the physics-informed neural network.

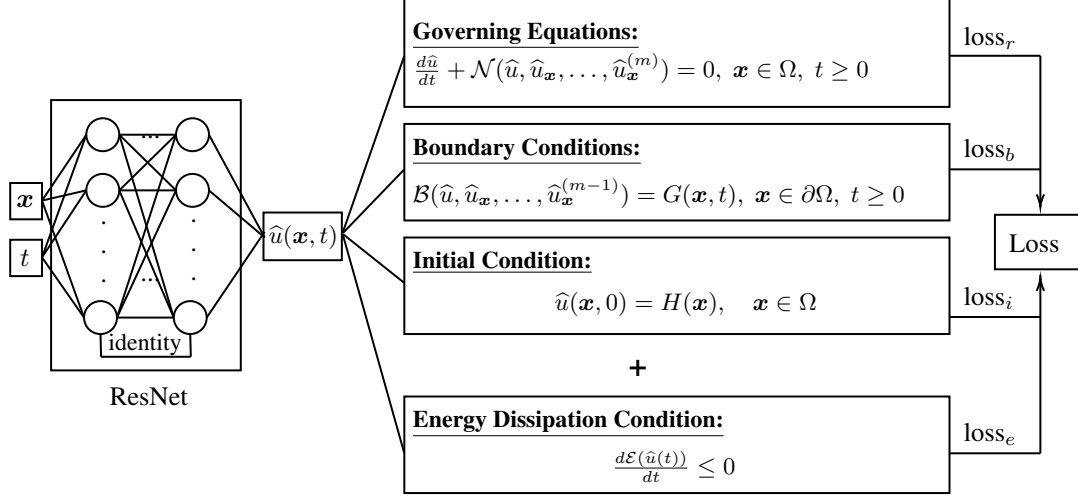


Figure 1: Workflow of the proposed PINN framework.

4.1 Adaptive sampling of collocation points

Phase field models as Allen-Cahn equation display sharp layers, where finer meshes are needed to capture the evolution dynamics in the traditional methods. Adaptive mesh refinement in the spatial domain has been considered as one of the effective approaches in the literature to obtain a better accuracy with the lower degrees of freedom for such kind of problems. Such a strategy has been also applied successfully during the training processes in the several studies; see, e.g., [31, 50, 77]. In a similar manner, we adaptively increase the number of collocation points by utilizing the residuals on the domain and boundary as an estimator; see Algorithm 1. This algorithm not only allows us to select samples

Algorithm 1 Adaptive Sampling of Collocation Points.

- 1: Randomly generate a new set of collocation points across the spatial domain

$$\mathcal{V} := \{(\mathbf{x}_k^v, t_k^v)\}_{k=1}^{n_v},$$

that is different from the current set of collocation points, denoted by \mathcal{T} .

- 2: Compute the PDE residuals η for the points in \mathcal{V} .
- 3: Find a subset $\mathcal{M} \subset \mathcal{V}$ with the smallest cardinality satisfying the bulk criteria [80]:

$$\tau \sum_{(\mathbf{x}_k^{v_r}, t_k^{v_r}) \in \mathcal{V}} \eta(\mathbf{x}_k^{v_r}, t_k^{v_r}) \leq \sum_{(\mathbf{x}_k^{v_r}, t_k^{v_r}) \in \mathcal{M} \subset \mathcal{V}} \eta(\mathbf{x}_k^{v_r}, t_k^{v_r}),$$

where $\tau \in (0, 1)$ is a bulk parameter.

- 4: Add the points in the set \mathcal{M} into the set \mathcal{T} , that is, $\mathcal{T} \leftarrow \mathcal{T} \cup \mathcal{M}$.
 - 5: Continue training with the updated collocation set \mathcal{T} .
-

from the sharp layers, but also to balance the computational cost by adaptively increasing the number of samples. On the other hand, due to the computations in the second line of the algorithm, we run the algorithm if the maximum of difference of loss values between last three successive iterations is greater than the given threshold tol_s , that is,

$$\max(L_k, L_{k-1}, L_{k-2}) \geq tol_s \quad \text{with} \quad L_k = \text{Loss}(\theta^k) - \text{Loss}(\theta^{k-1}), \quad (16)$$

and number of executed epochs is greater than a level denoted by $n_{ex} = 1000$. The size of new data, n_v , is also taken as %20 of the current training points.

4.2 Adaptivity in the temporal domain

As done in the spatial domain, it is also possible to take advantages of adaptivity in the temporal domain; see, e.g., [65, 50]. In this setting, separate networks for each time interval with the given time step Δt are constructed. For the first network, we use the given initial condition $H(x)$. For the next time intervals, the predicted solution \hat{u} in the

previous time segment is used as the initial condition. Algorithm 2 summarizes the adaptivity process in the temporal domain.

Algorithm 2 Adaptive Time Strategy.

```

1: Given the time step  $\Delta t$  and maximum iteration number  $N_{max}$ .
2: Set  $t_0 = 0$ .
3: for  $j = 1 \dots N_{max}$  do
4:   Set  $t_j = t_{j-1} + \Delta t$  and  $I_j = [t_{j-1}, t_j]$ .
5:   if  $(j = 1)$  then
6:     Set  $H(x)$  as an initial condition for the interval  $I_j$ .
7:   else
8:     Set the solution  $\hat{u}(x, t_{j-1})$  as an initial condition for the interval  $I_j$ .
9:   end if
10:  Create a neural network on  $I_j$  and predict the solution  $\hat{u}(x, t_j)$  by using the trained neural network.
11: end for

```

5 Numerical experiments

In this section, we will examine the effectiveness of the proposed energy dissipation approach outlined in Section 3 and compare it with existing studies in the literature.

Unless otherwise states, the hyperparameters used in the simulations are described in Table 1. Hyperparameters are key settings that significantly affect a model’s performance. Consequently, hyperparameter optimization, which involves identifying the optimal combination of these settings to either minimize or maximize an objective function such as training loss or model accuracy, is essential. This optimization can be achieved through automated techniques like OPTUNA [81], grid search [82], Bayesian optimization [83], or by employing a manual tuning strategy [84, 85]. However, in this study, when deciding some of the hyperparameters, we consider the physical properties of the underlying partial differential equation (PDE), including its nonlinearity, time dependence, and the one-dimensional analytical solution for the transition layer, which describes the shift between the stable states $u = \pm 1$, that is, $u = \tanh\left(\frac{x-x_0}{\sqrt{2}\epsilon}\right)$ for any arbitrary point x_0 in the domain. We prefer to use ResNet network structure [86] due to its advantages in combining low-level and high-level features in the learning process. To take advantages of both ADAM (first-order method) and L-BFGS (second-order method), we here apply ADAM+L-BFGS strategy as optimizer [31], which means that ADAM is applied until a certain number of iterations and then switched to L-BFGS method. As suggested in [87], the learning rate of ADAM optimizer is 0.001 with all other parameters. With the help of this hybrid approach, ADAM can handle the initial exploration and rapid convergence, while L-BFGS can refine the solution by leveraging its second-order information. In the test examples, we have two pure states for the solution and the solution approaches one of them over time. Therefore, the hyperbolic tangent \tanh is taken as an activation function by considering its success in the two-class classification problems and the behaviour of the analytical solution for the transition layer. The activation function of the output layer, that is, σ_L , is a affine transformation for polynomial potentials, while for logarithmic potentials, it is the hyperbolic tangent function \tanh . To sample training points, we use Latin hypercube sampling [75] for all cases. Further, all the neural networks are trained on Intel Core i7-6700 CPU 3.40GHz and 16 GB RAM. The software packages used for all simulations are Tensorflow 1.14 and MATLAB R2021a, and the data type of all the variables are float32. We note that the computations have been conducted on Central Processing Units (CPUs) due to resource constraints. However, for machine learning (ML) tasks, utilizing Graphical Processing Units (GPUs) can be more advantageous since GPUs are specifically designed to break down complex problems into thousands of smaller tasks and process them simultaneously.

Table 1: Hyperparameters used in the simulations.

Hyperparameters	Used approaches
Network structure	residual neural network (ResNet) [86]
Initialization of weights	Xavier initialization [72]
Sampling of points	Latin hypercube sampling [75]
Activation function	hyperbolic tangent \tanh
Optimizer	ADAM + L-BFGS [31]

In the numerical simulations, we begin by comparing the performance of our method with the existing PINN approaches from the literature using a well-studied example. To test accuracy of the obtained solution on the testing points, we use

a relative total error over the entire domain as done in [32, 50, 65]

$$error = \frac{\left(\frac{1}{n} \sum_{i=1}^n |u_r(\mathbf{x}_i, t_i) - \hat{u}(\mathbf{x}_i, t_i)|^2\right)^{1/2}}{\left(\frac{1}{n} \sum_{i=1}^n |u_r(\mathbf{x}_i, t_i)|^2\right)^{1/2}},$$

where u_r is the analytic solution (if exists); otherwise, it is a reference solution, and $\{(\mathbf{x}_i, t_i)\}_{i=1}^n$ are test data points, which correspond to the grid points here. In the rest of simulations, the proposed approach will be tested by using various forms of the Allen-Cahn equation to demonstrate that the predicted solutions align with existing literature and adhere to the maximum bound principle, particularly ensuring the energy dissipation.

5.1 1D Allen–Cahn with polynomial potential

As a first benchmark problem, we consider one-dimensional Allen-Cahn equation with the periodic boundary conditions and the quartic double-well potential energy (5), formulated as follows

$$\begin{aligned} u_t - 0.0001u_{xx} + 5(u^3 - u) &= 0, & \mathbf{x} &\in [-1, 1], \quad t \in [0, T], \\ u(\mathbf{x}, 0) &= \mathbf{x}^2 \cos(\pi \mathbf{x}), \\ u(-1, t) &= u(1, t), \\ u_x(-1, t) &= u_x(1, t). \end{aligned} \tag{17}$$

In this example, we aim to compare the performance of our methodology with various PINN variants used to solve the benchmark problem in (17). As done in the studies [32, 50, 65], a reference solution is obtained by using spectral methods with the Chebfun package [88]. To ensure a fair comparison with existing studies in the literature, hyperparameters are kept as consistent as possible; see, Table 2 for the used hyperparameters in this example.

Table 2: Description of training data for the Example 5.1.

Parameters	Values	Descriptions
NN depth	4	# hidden layer
NN width	100	# neurons in each hidden layer
(n_r, n_b, n_i)	(500, 42, 128)	size of initial samples per time segment
$(\lambda_r, \lambda_b, \lambda_i, \lambda_e)$	(1, 1, 100, 542)	scale parameters in (15)
(τ, tol_s)	$(0.1, 5 \times 10^{-2})$	parameters used in Algorithm 1
(Δ_t, N_{max})	(0.1, 20)	parameters used in Algorithm 2
(N_{Adam}, N_{LBFGS})	(5000, 5000)	maximum ADAM and L-BFGS iterations per time segment

Table 3: Performance comparison for the Example 5.1.

method	relative ℓ_2 -norm
std-PINN [32]	0.9919
XPINN [48]	0.9612
bc-PINN [65]	0.0701
bc-PINN + logresidual [65]	0.0300
ACP [50]	0.0233
bc-PINN + ICGL + TL [65]	0.0168
AT + ACP	0.0078
AT + ACP + Energy Penalty	0.0053

In Table 3, we compare the different approaches in the literature with our approach by taking the final time $T = 1$. By comparing with std-PINN, XPINN, bc-PINN, bc-PINN + logresidual, and bc-PINN + ICGL + TL produced in [65] with 4 hidden layer, 200 neurons in each layer, 512 points for initial condition, 201 points for the boundary condition, 20,000 collocation points for the residual per time segment, and with ACP produced in [50] with 4 hidden layer, 128 neurons in each layer, 512 points for initial condition, 200 points for the boundary condition, 10,000 collocation points for the residual, our proposed approach makes a significant improvement accuracy in spite of lower sampling points (less than 14,000 sampling points in total).

Figure 2 presents a comparison between the predicted solution, \hat{u} , and the reference solution, u_r , obtained using Chebfun. Although, the error increases with time slowly in Figure 3, it is observed that their behaviours are almost

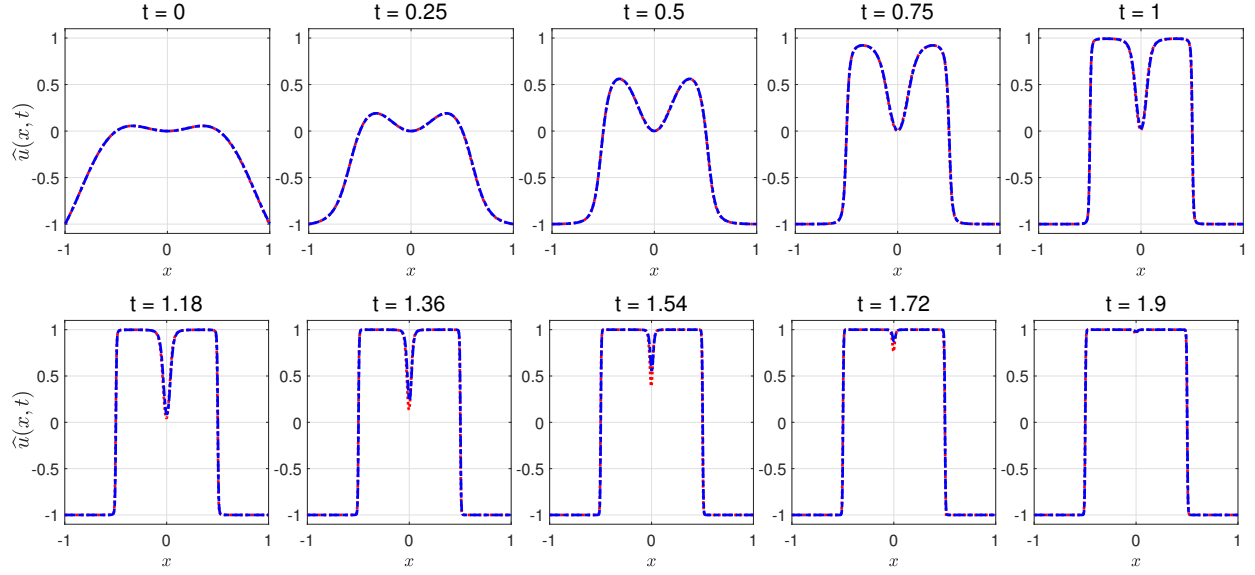


Figure 2: Example 5.1: Predicted $\hat{u}(x, t)$ (red) and reference $u_r(x, t)$ (blue) solutions at various time slots.

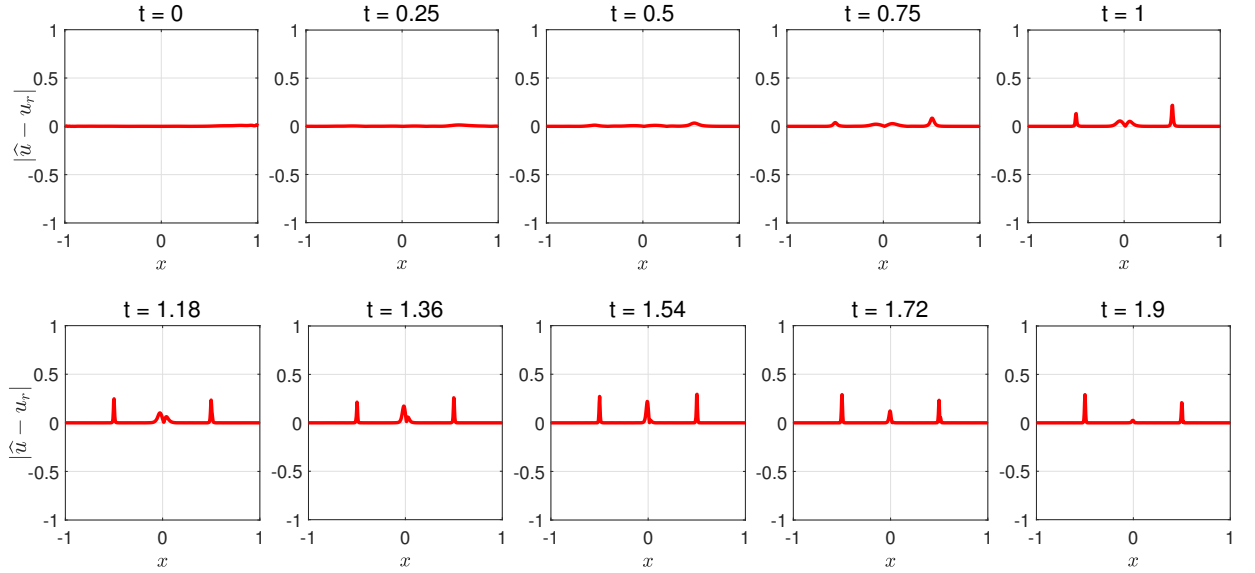


Figure 3: Example 5.1: Behaviour of absolute error $|\hat{u} - u_r|$ at various time slots.

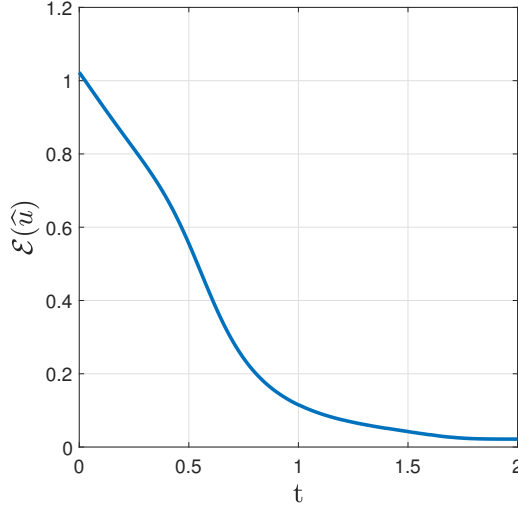


Figure 4: Example 5.1: Time evolution of the predicted energy functional $\mathcal{E}(\hat{u})$.

similar. In addition, our predicted solution stays bounded on $[-1, 1]$, which implies that the maximum bound principle is satisfied. Last, the behaviour of the predicted energy functional $\mathcal{E}(\hat{u})$ is given in Figure 4. As expected, it satisfies the decay of energy condition over time.

5.2 2D Allen–Cahn with polynomial potential

Next, we consider a two dimensional Allen-Cahn equation with the quartic double-well potential energy (5), in the form of

$$\begin{aligned} u_t &= \mu(u)(\epsilon^2 \Delta u - u^3 + u), & \mathbf{x} \in \Omega, \quad t \in [0, T], \\ \frac{\partial u}{\partial \mathbf{n}} &= 0, & \mathbf{x} \in \partial\Omega, \\ u(\mathbf{x}, 0) &= \tanh\left(\frac{0.35 - \sqrt{(x_1 - 0.5)^2 + (x_2 - 0.5)^2}}{2\epsilon}\right), & \mathbf{x} \in \Omega, \end{aligned}$$

where $\Omega = [0, 1]^2$, $\epsilon = 0.025$, and $\mu(u) = 10$. Hyperparameters used in this example are displayed in Table 4.

Table 4: Description of training data for the Example 5.2.

Parameters	Values	Descriptions
NN depth	6	# hidden layer
NN width	128	# neurons in each hidden layer
(n_r, n_b, n_i)	(5000, 200, 2601)	size of initial samples per time segment
$(\lambda_r, \lambda_b, \lambda_i, \lambda_e)$	(1, 1, 1000, 5200)	scale parameters in (15)
(τ, tol_s)	(0.05, 10^{-2})	parameters used in Algorithm 1
(Δ_t, N_{max})	(0.25, 40)	parameters used in Algorithm 2
(N_{Adam}, N_{LBFGS})	(5000, 2000)	maximum ADAM and L-BFGS iterations per time segment

Unlike the previous one-dimensional example, the trained weights and biases from the earlier time segment are transferred to the current time segment and serve as initials for the remaining test examples; see, e.g., [89]. It is seen from Figure 5 that the two-phases, $u = -1$ and $u = 1$, start moving and finally reaches the phase $u = -1$. As time moves forward, the circles shrink with time to the center of the circle as expected; see, e.g., [66, 90]. The decay of the energy functional $\mathcal{E}(\hat{u})$ over time is displayed in Figure 6. In Figure 7, we also investigate the performance the adaptive collocation approach in Algorithm 1. We notice that the adaptive collocation points are densely concentrated around the circle, which seems consistent with the results in Figure 5.

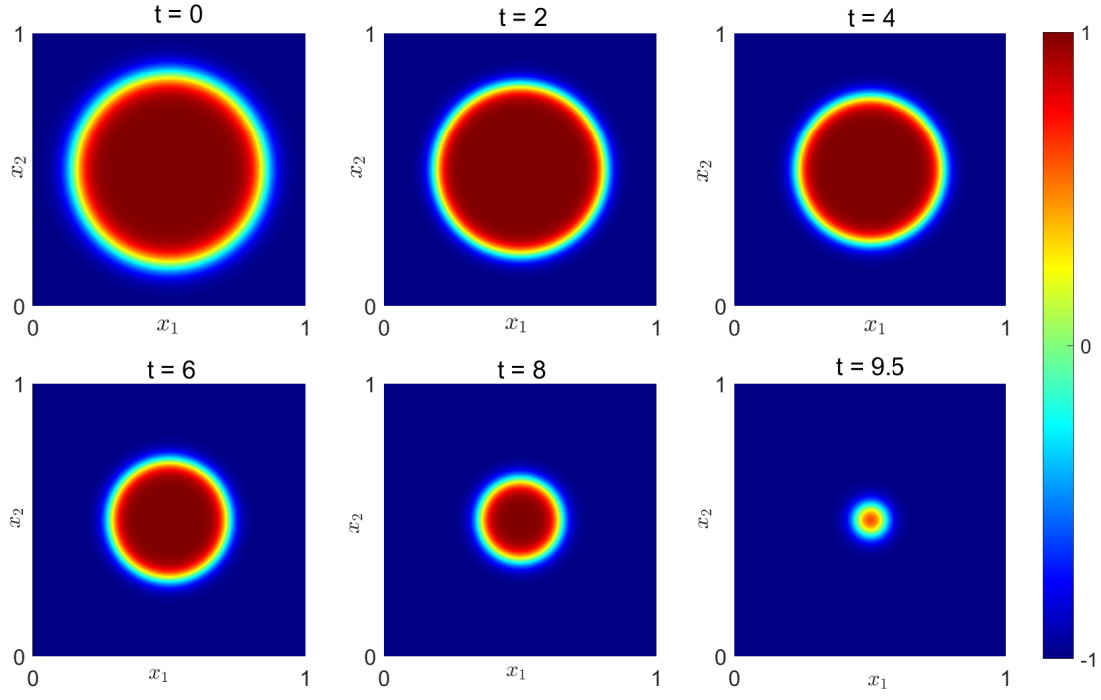


Figure 5: Example 5.2: Predicted solutions $\hat{u}(x, t)$ obtained by the proposed methodology at various time slots.

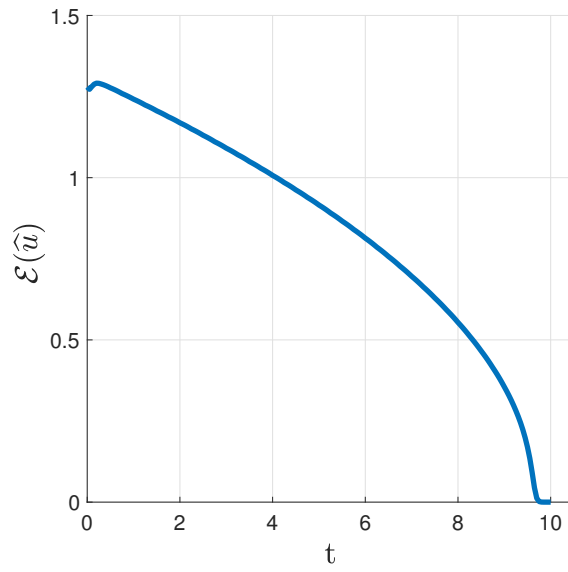


Figure 6: Example 5.2: Time evolution of the predicted energy functional $\mathcal{E}(\hat{u})$.

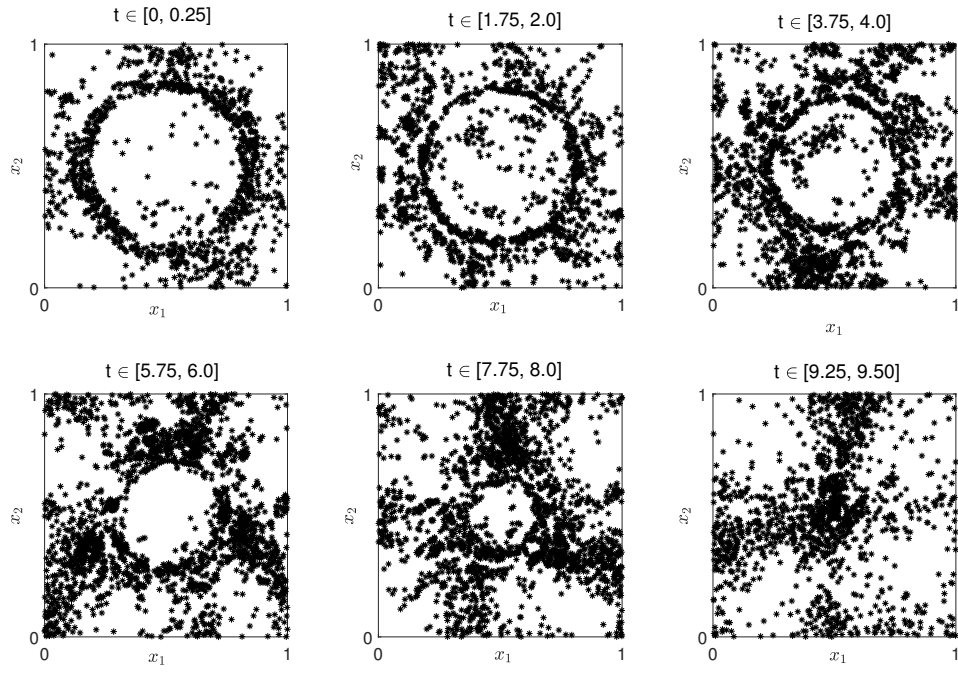


Figure 7: Example 5.2: Distribution of adaptive collocation points at various time intervals.

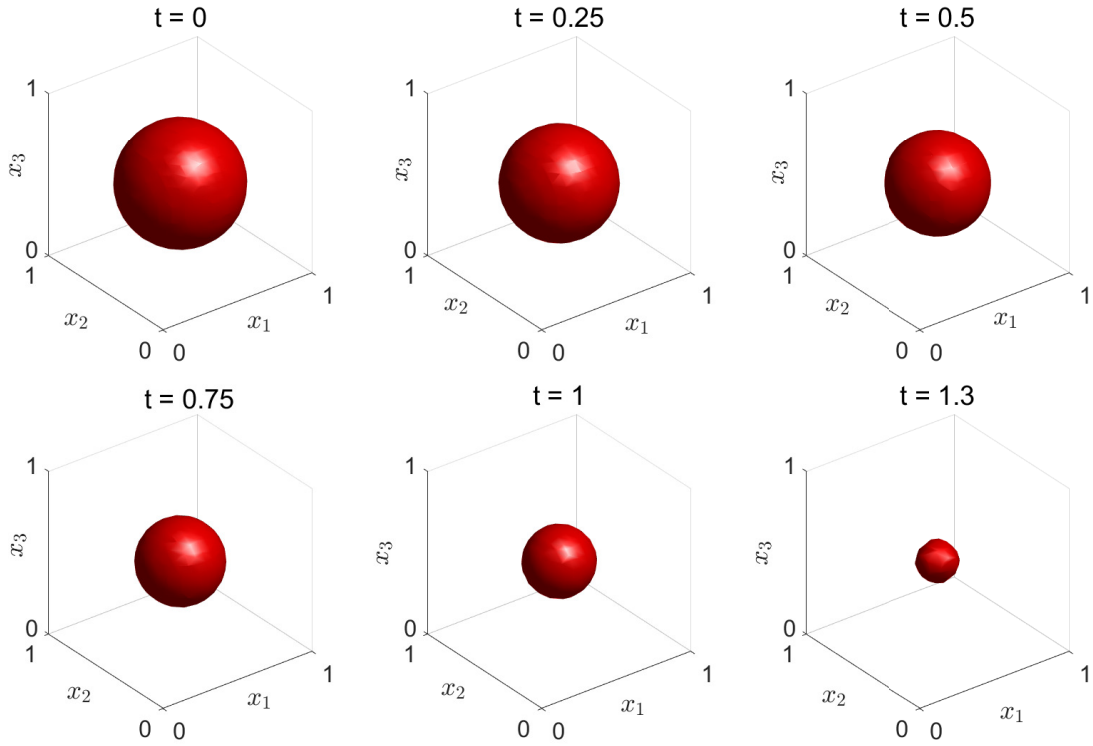


Figure 8: Example 5.3: Predicted solutions $\hat{u}(x, t)$ obtained by the proposed methodology at various time slots.

5.3 3D Allen–Cahn with polynomial potential

This example is an extension of the previous two dimensional Example 5.2 into the domain $\Omega = [0, 1]^3$ with the parameters $\epsilon = 0.05$, $\mu(u) = 10$, and the initial condition

$$u(\mathbf{x}, 0) = \tanh \left(\frac{0.35 - \sqrt{(x_1 - 0.5)^2 + (x_2 - 0.5)^2 + (x_3 - 0.5)^2}}{2\epsilon} \right).$$

Table 5: Description of training data for the Example 5.3.

Parameters	Values	Descriptions
NN depth	6	# hidden layer
NN width	128	# neurons in each hidden layer
(n_r, n_b, n_i)	(5000, 300, 9261)	size of initial samples per time segment
$(\lambda_r, \lambda_b, \lambda_i, \lambda_e)$	(1, 1, 1000, 5300)	scale parameters in (15)
(τ, tol_s)	$(0.05, 10^{-2})$	parameters used in Algorithm 1
(Δ_t, N_{max})	(0.1, 13)	parameters used in Algorithm 2
(N_{Adam}, N_{LBFGS})	(5000, 2000)	maximum ADAM and L-BFGS iterations per time segment

Table 5 shows the used parameters in the simulation. Figure 8 exhibits the zero isosurface of the solution at various time levels. Over time the size of the sphere decreases, which is also observed in [66, 90]. As expected, the predicted energy functional decreases $\mathcal{E}(\hat{u})$ as time increases; see, Figure 9.

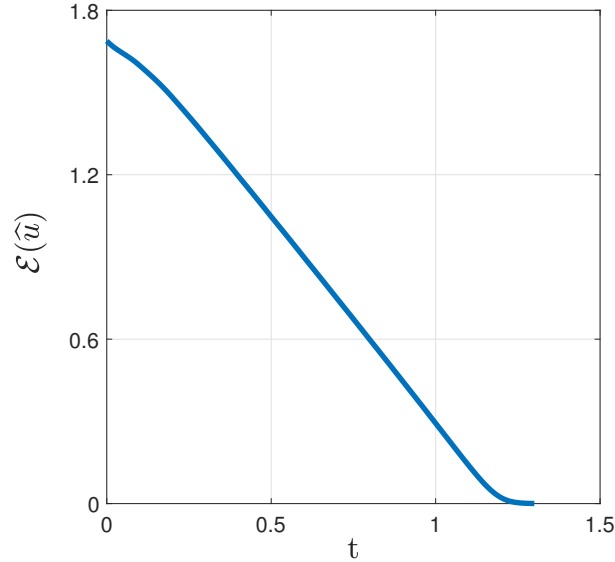


Figure 9: Example 5.3: Time evolution of the predicted energy functional $\mathcal{E}(\hat{u})$.

5.4 2D Allen–Cahn with logarithmic potential

Now, we consider a 2D Allen-Cahn equation (3) with logarithmic potential (4) on the domain $\Omega = [0, 2\pi]^2$, taken from [91]. Rest of data is taken as

$$\mu(u) = 1, \quad \epsilon = 0.1, \quad \theta_c = 1, \quad \theta = \frac{1}{4},$$

and the initial condition consisting of seven circles

$$u(\mathbf{x}, 0) = -1 + \sum_{i=1}^7 h \left(\sqrt{(x_1 - a_i)^2 + (x_2 - b_i)^2} - r_i \right), \quad (18)$$

where

$$h(s) = \begin{cases} 2e^{-\epsilon^2/s^2}, & \text{if } s < 0, \\ 0, & \text{otherwise,} \end{cases}$$

and circles' centers and radii are given in Table 6. Further, periodic boundary conditions are considered in this example; see Table 7 for the rest of used parameters in the simulation.

Table 6: Centers (a_i, b_i) and radii r_i in the initial condition (18) of the Example 5.4.

i	1	2	3	4	5	6	7
a_i	$\pi/2$	$\pi/4$	$\pi/2$	π	$3\pi/2$	π	$3\pi/2$
b_i	$\pi/2$	$3\pi/4$	$5\pi/4$	$\pi/4$	$\pi/4$	π	$3\pi/2$
r_i	$\pi/5$	$2\pi/15$	$2\pi/15$	$\pi/10$	$\pi/10$	$\pi/4$	$\pi/4$

Table 7: Description of training data for the Example 5.4.

Parameters	Values	Descriptions
NN depth	6	# hidden layer
NN width	128	# neurons in each hidden layer
(n_r, n_b, n_i)	(10000, 200, 40401)	size of initial samples per time segment
$(\lambda_r, \lambda_b, \lambda_i, \lambda_e)$	(1, 1, 1000, 10200)	scale parameters in (15)
(τ, tol_s)	(0.05, 10^{-1})	parameters used in Algorithm 1
(Δ_t, N_{max})	(0.125, 40)	parameters used in Algorithm 2
(N_{Adam}, N_{LBFGS})	(5000, 2000)	maximum ADAM and L-BFGS iterations per time segment

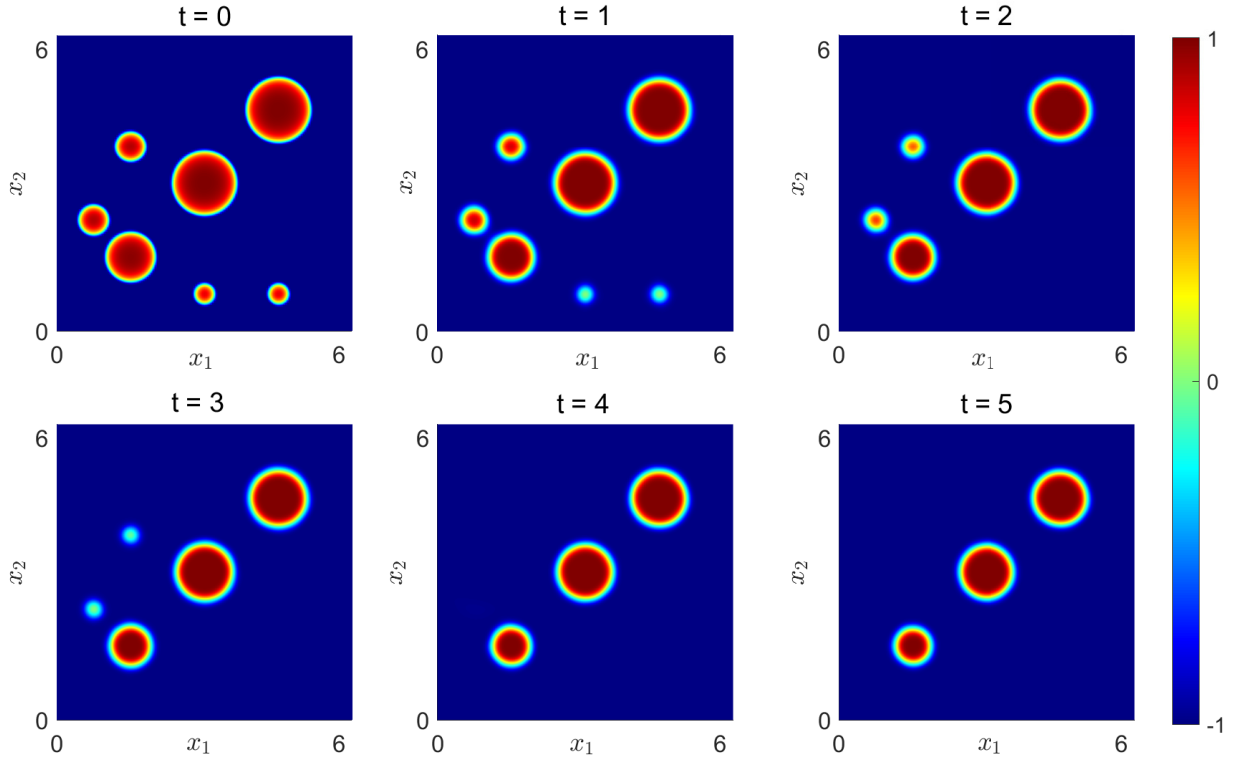


Figure 10: Example 5.4: Predicted solutions $\hat{u}(x, t)$ obtained by the proposed methodology at various time slots.

From the predicted solutions in Figure 10, it is seen that the circles annihilate gradually in time as observed in [91]. The behaviour of the approximated energy functional $\mathcal{E}(\hat{u})$ is displayed in Figure 11. It seems that our approach results in a progressively diminishing estimated energy. Last, Figure 12 shows that the distribution of adaptive collocation points become intense around the circles as expected from the results in Figure 10.

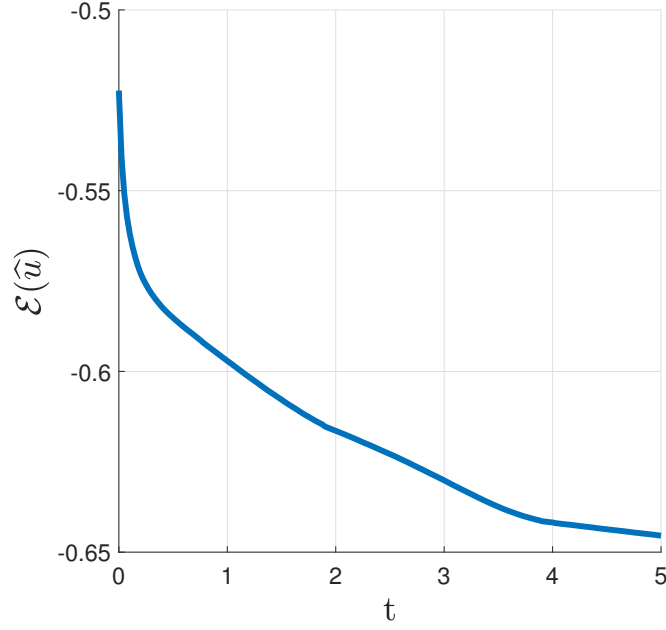


Figure 11: Example 5.4: Time evolution of the predicted energy functional $\mathcal{E}(\hat{u})$.

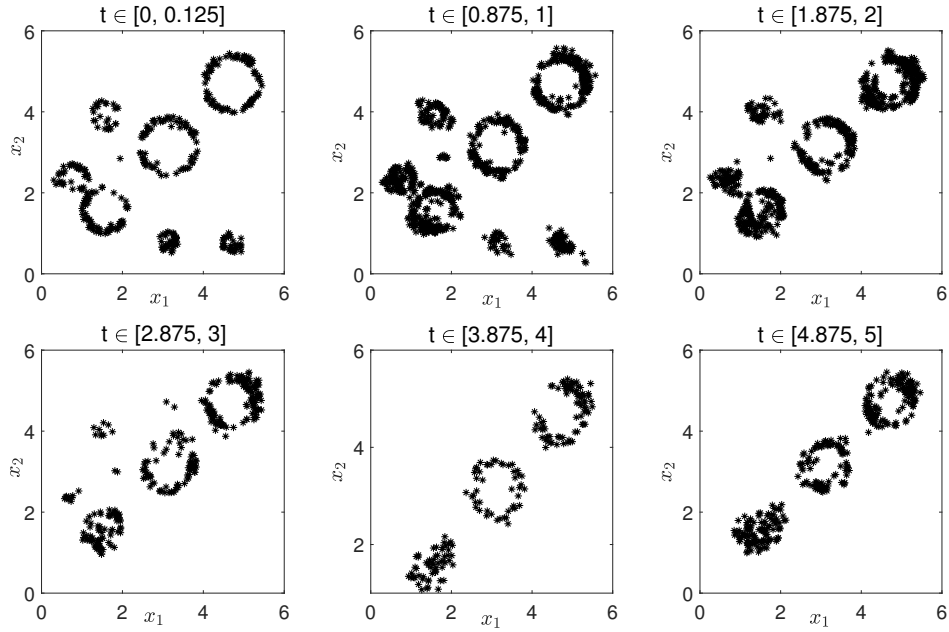


Figure 12: Example 5.4: Distribution of adaptive collocation points at various time intervals.

5.5 2D Allen–Cahn with logarithmic potential and random initials

Next, we consider a benchmark example (3) with the logarithmic free energy (4), periodic boundary conditions, and a random initial condition

$$u_0(x, 0) = 0.05(2 \times \text{randn} - 1)$$

on the domain $\Omega = [0, 2\pi]^2$, taken from [92]. Here, `randn` generates normally distributed random vector. The rest of the problem data are

$$\mu(u) = 2, \quad \epsilon = 0.04, \quad \theta = 0.15, \quad \theta_c = 0.30.$$

Different from the previous examples, the learning process of the initial condition is not straightforward due to its inherent randomness. As a remedy, we use a continuous analogue of the initial random vector. For a complex periodic smooth random function on the domain $[-L/2, L/2]^2$ with $L > 0$, its continuous analogue is characterized by a finite Fourier series with independent normally distributed random coefficients

$$f(x, y) = \sum_{k=-m}^m \sum_{j=-m_k}^{m_k} c_{jk} \exp\left(\frac{2\pi i(jx + ky)}{L}\right), \quad (19)$$

where $m = \lfloor L/\gamma \rfloor$ with a wavelength parameter $\gamma > 0$ and $m_k = \sqrt{m^2 - k^2}$. The coefficient parameters, c_{jk} , are the element of a $(2m + 1) \times (2m_k + 1)$ matrix that includes independent sample from a normal distribution. We construct the corresponding smooth initial condition by using `randnfun2` built-in function in the Chebfun package [88], regarded as a continuous analogue of the MATLAB command `randn`. We refer to [93] for a more detailed discussion. In the simulations, the wavelength parameter γ is taken as $\gamma = 1$. It is not presented here but different values of γ yields similar behaviours.

Table 8: Description of training data for the Example 5.5.

Parameters	Values	Descriptions
NN depth	6	# hidden layer
NN width	128	# neurons in each hidden layer
(n_r, n_b, n_i)	(5000, 200, 40000)	size of initial samples per time segment
$(\lambda_r, \lambda_b, \lambda_i, \lambda_e)$	(1, 1, 1000, 5200)	scale parameters in (15)
(τ, tol_s)	(0.05, 0.1)	parameters used in Algorithm 1
(Δ_t, N_{max})	(1, 20)	parameters used in Algorithm 2
(N_{Adam}, N_{LBFGS})	(5000, 2000)	maximum ADAM and L-BFGS iterations per time segment

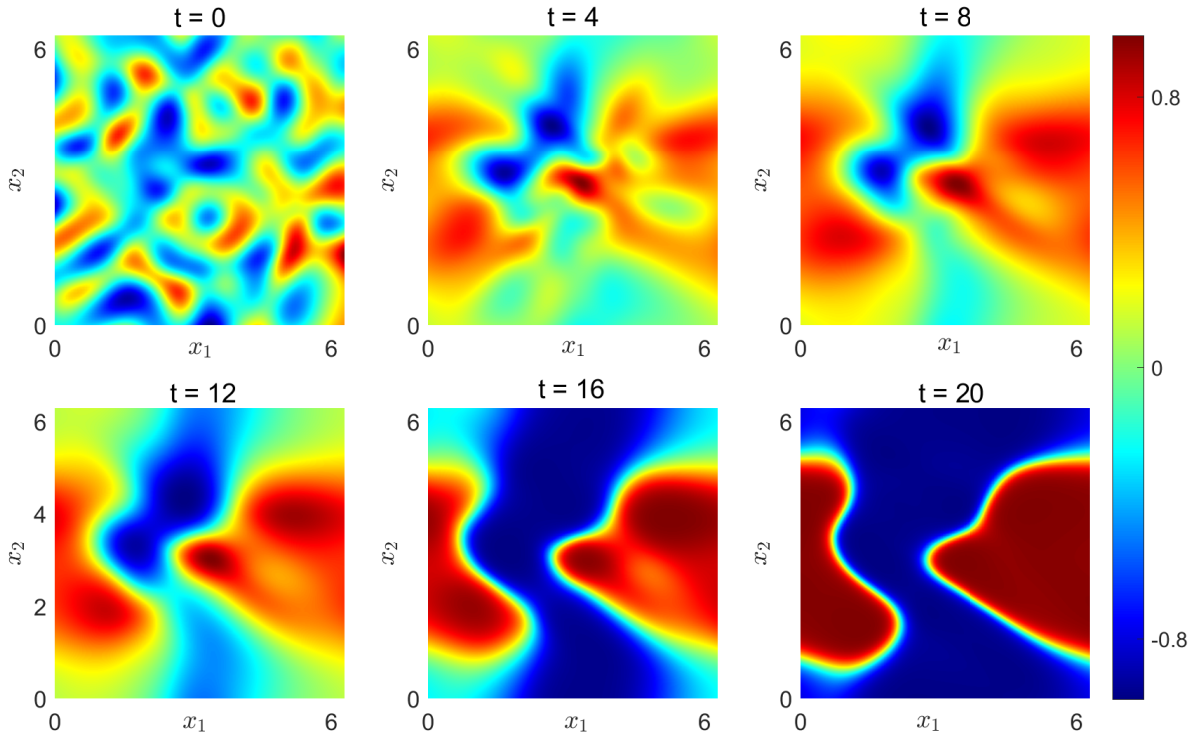


Figure 13: Example 5.5: Predicted solutions $\hat{u}(x, t)$ obtained by the proposed methodology at various time slots.

Table 8 displays the parameters used in the training of the network. From Figure 13, it is seen that the our approach yields a coarsening phenomenon during the phase evolution as expected; see also [92]. In addition, the predicted

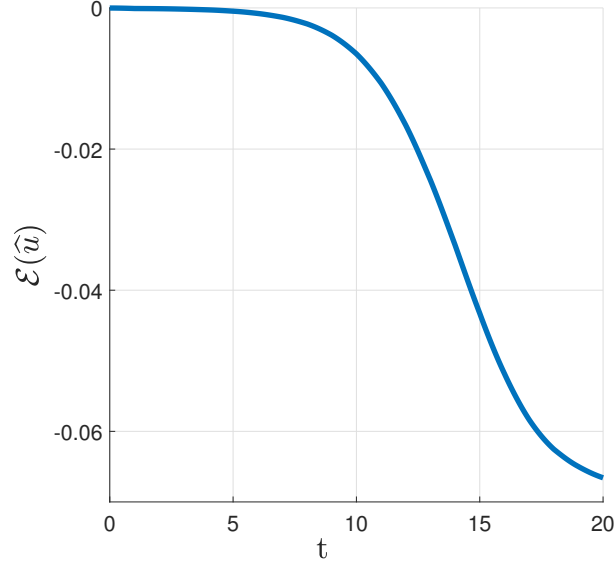


Figure 14: Example 5.5: Time evolution of the predicted energy functional $\mathcal{E}(\hat{u})$.

solutions $\hat{u}(x, t)$ is bounded in the interval $[-s, s]$ for all the time, where $1 > s > 0$ is the constant satisfying $f(s) = 0$. It implies that the discrete maximum principle are indeed well satisfied. Further, the decay of energy function is displayed in Figure 14.

Table 9: Description of training data for the Example 5.6.

Parameters	Values	Descriptions
NN depth	6	# hidden layer
NN width	128	# neurons in each hidden layer
(n_r, n_b, n_i)	(7500, 200, 40.000)	size of initial samples per time segment
$(\lambda_r, \lambda_b, \lambda_i, \lambda_e)$	(1, 1, 10^5 , 7700)	scale parameters in (15)
(τ, tol_s)	(0.05, 0.1)	parameters used in Algorithm 1
(Δ_t, N_{max})	(1, 10)	parameters used in Algorithm 2
(N_{Adam}, N_{LBFGS})	(3000, 20.000)	maximum ADAM and L-BFGS iterations per time segment

5.6 2D Allen–Cahn with logarithmic potential and degenerate mobility

Now we examine a two-dimensional Allen-Cahn equation characterized by the logarithmic potential (4), random initial condition, and degenerate mobility function within the domain $\Omega = [0, 2\pi]^2$. The functions and parameters of the underlying problem, taken from [19, 92], are

$$\epsilon = 0.04, \quad \theta_c = 0.95, \quad \theta = 0.5, \quad \mu = 2(1 - u^2),$$

with the random initial condition

$$u(\mathbf{x}, 0) = 0.05(2 \times \text{randn} - 1).$$

As the previous example, we construct a continuous analogue of the random initial condition with the wavelength parameter $\gamma = 0.4$. To address the challenge posed by the nonlinear mobility function, we adopt a strategy similar to explicit-implicit methods used in the numerical analysis. Instead of directly dealing with the nonlinear mobility function, we utilize the predicted solutions from the previous time step in the Algorithm 2. Figure 15 illustrates the temporal behavior of the predicted solutions utilizing the parameters outlined in Table 9. The results show that a spinodal decomposition happens over time and the predicted solutions $\hat{u}(x, t)$ preserve the boundedness. Figure 16 also displays that the approximate energy functional $\mathcal{E}(\hat{u})$ is dissipated.

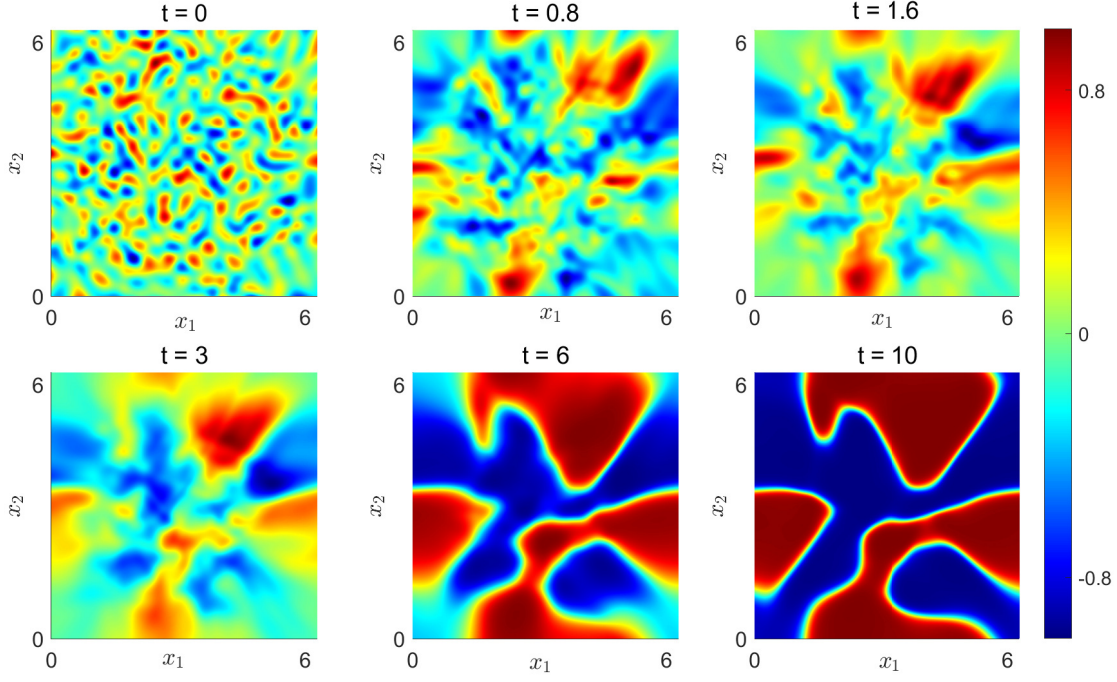


Figure 15: Example 5.6: Predicted solutions $\hat{u}(x, t)$ obtained by the proposed methodology at various time slots.

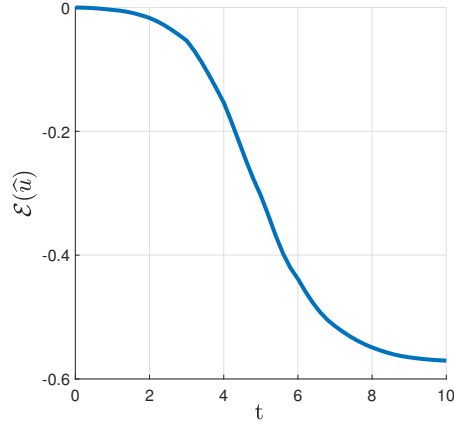


Figure 16: Example 5.6: Time evolution of the predicted energy functional $\mathcal{E}(\hat{u})$.

Table 10: Description of training data for the Example 5.7.

Parameters	Values	Descriptions
NN depth	6	# hidden layer
NN width	128	# neurons in each hidden layer
(n_r, n_b, n_i)	(10000, 200, 10201)	size of initial samples per time segment
$(\lambda_r, \lambda_b, \lambda_i, \lambda_e)$	(1, 1, 10^5 , 10200)	scale parameters in (15)
(τ, tol_s)	(0.05, 0.1)	parameters used in Algorithm 1
(Δ_t, N_{max})	(0.005, 12)	parameters used in Algorithm 2
(N_{Adam}, N_{LBFGS})	(5000, 2000)	maximum ADAM and L-BFGS iterations per time segment

5.7 2D Allen–Cahn with advection and polynomial potential

Last, we consider an advective Allen–Cahn equation under homogeneous Neumann boundary condition, taken from [94], in the form of

$$\begin{aligned} u_t &= \mu(u)(\epsilon^2 \Delta u - u^3 + u) - \beta \cdot \nabla u, & \mathbf{x} \in \Omega, \quad t \in [0, T], \\ \frac{\partial u}{\partial \mathbf{n}} &= 0, & \mathbf{x} \in \partial\Omega, \\ u(\mathbf{x}, 0) &= -\tanh\left(\frac{|x_1 + x_2 - 1| + |x_1 - x_2| - 0.1}{\sqrt{2}\epsilon}\right), & \mathbf{x} \in \Omega, \end{aligned}$$

where $\Omega = [0, 1]^2$, $\mu(u) = 100$, $\epsilon = 0.01$, $\beta = (0, -100(x_1 - 0.5))^T$, and $T = 0.06$. Training parameters are given in Table 10. We present the evolution of the predicted phase function \hat{u} in Figure 17. From the results it is seen that the maximum bound principle is satisfied. The similar numerical results were also observed in [94]. Due to the advection term, we update the energy function as follows [95]

$$\mathcal{E}_\beta(u) = \int_{\Omega} \left(\frac{\epsilon^2}{2} |\nabla u|^2 + F(u) + \frac{1}{2} |\beta|^2 \right) dx,$$

where the last term represents the kinetic energy density associated to the vector field β . Then, the predicted energy function $\mathcal{E}_\beta(\hat{u})$, exhibited in Figure 18, is decreasing over time as expected.

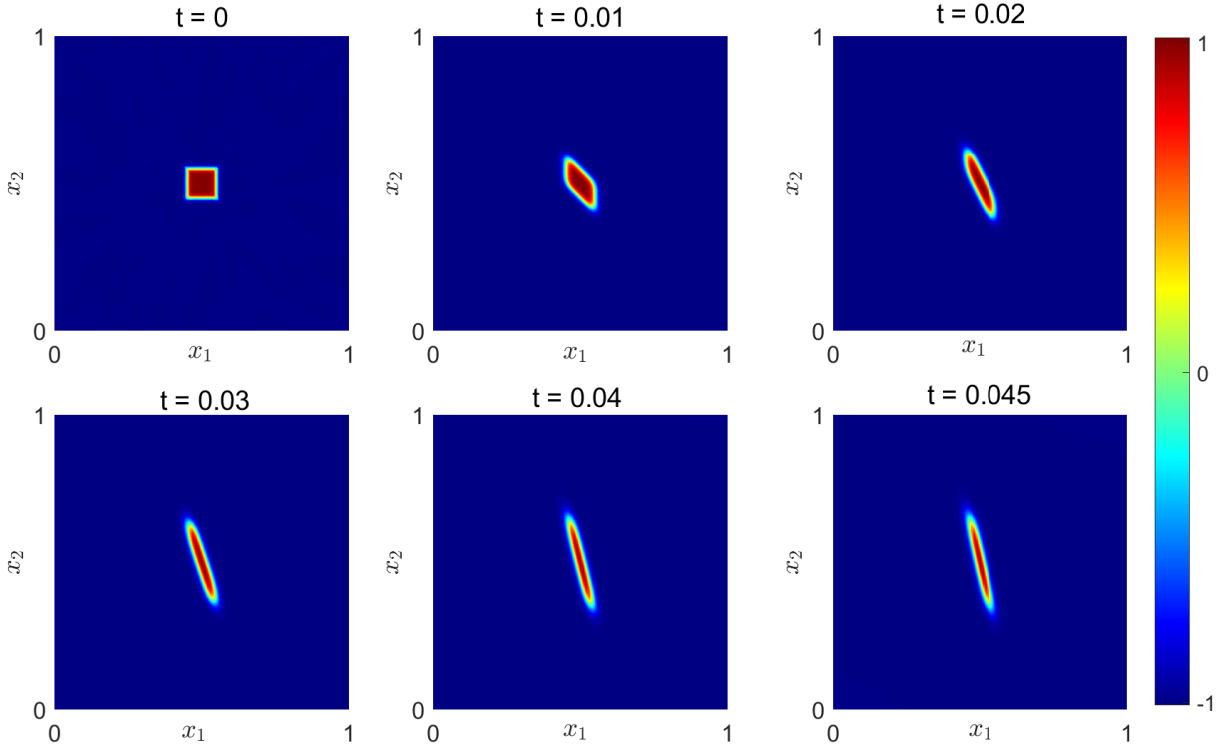


Figure 17: Example 5.7: Predicted solutions $\hat{u}(x, t)$ obtained by the proposed methodology at various time slots.

6 Conclusion

In this paper, we have proposed a modified physics-informed neural network (PINN) approach to solve the Allen–Cahn equation by imposing the energy dissipation condition as a penalty term into the loss function of the network. A comprehensive numerical experiments including various types of benchmark examples have been conducted to illustrate the outstanding performance of our proposed approach, including its dynamics prediction and generalization ability

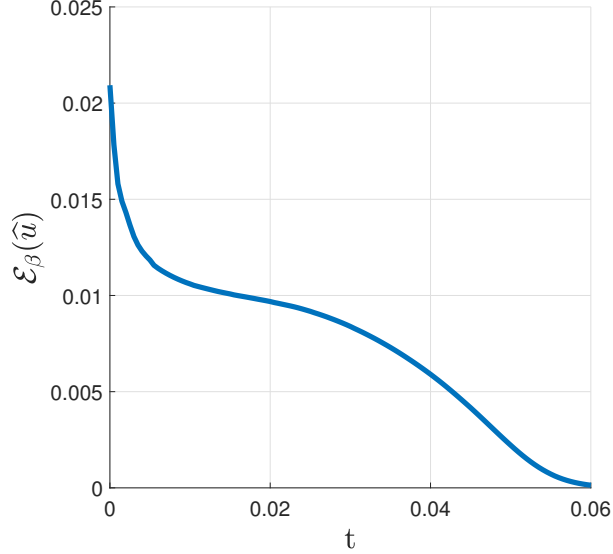


Figure 18: Example 5.7: Time evolution of the predicted energy functional $\mathcal{E}_\beta(\hat{u})$.

under different scenarios. To address the challenge of learning random initial conditions, we substitute them with a continuous and smooth analogue using the Fourier series expansion. Numerical results consistently show a decrease in discrete energy, while also highlighting phenomena like phase separation. Overall, it is evident that deep learning techniques, like PINN, offer appealing alternatives for solving complex engineering challenges.

The code associated with this manuscript is available in a GitHub repository:
https://github.com/mustafakutuk/AC_PINN.

Acknowledgements

The authors would like to express their sincere thanks to the anonymous referees for their most valuable suggestions. HY gratefully acknowledges the research support provided by the Scientific and Technological Research Council of Turkey (TUBITAK) under the program TUBITAK 2219-International Postdoctoral Research Fellowship (Project No: 1059B192302207) and would like to thank the Max Planck Institute for Dynamics of Complex Technical Systems, Magdeburg for its excellent hospitality.

References

- [1] I. Steinbach. Phase-field models in materials science. *Model. Simul. Mat. Sci. Eng.*, 17(7):073001, 2009.
- [2] J. Kim. Phase-field models for multi-component fluid flows. *Commun. Comput. Phys.*, 12(3):613–661, 2012.
- [3] A. Karma, D. A. Kessler, and H. Levine. Phase-field model of mode III dynamic fracture. *Phys. Rev. Lett.*, 87(4):1–4, 2001.
- [4] B. Bourdin, G. A. Francfort, and J-J. Marigo. Numerical experiments in revisited brittle fracture. *J. Mech. Phys. Solids*, 48(4):797–826, 2000.
- [5] Y. Li and J. Kim. Multiphase image segmentation using a phase-field model. *Comput. Math. Appl.*, 62(2):737–745, 2011.
- [6] M. Brassel and E. Bretin. A modified phase field approximation for mean curvature flow with conservation of the volume. *Math. Methods Appl. Sci.*, 34(10):1157–1180, 2011.
- [7] S. M. Allen and J. W. Cahn. A microscopic theory for antiphase boundary motion and its application to antiphase domain coarsening. *Acta Metall.*, 27:1159–1180, 1979.
- [8] J. W. Barrett, J. F. Blowey, and H. Garcke. Finite element approximation of the Cahn-Hilliard equation with degenerate mobility. *SIAM J. Numer. Anal.*, 37(1):286–318, 2000.

- [9] M. J. Ward. Metastable bubble solutions for the Allen-Cahn equation with mass conservation. *SIAM J. Appl. Math.*, 56(5):1247–1279, 1996.
- [10] P. de Mottoni and M. Schatzma. Geometrical evolution of developed interfaces. *Trans. Amer. Math. Soc.*, 347(5):1533–1589, 1995.
- [11] L. Bronsard and R. V. Kohn. Motion by mean curvature as the singular limit of Ginzburg-Landau dynamics. *J. Differ. Equ.*, 90(2):211–237, 1991.
- [12] L. Q. Chen. Phase-field models for microstructure evolution. *Ann. Rev. Mater. Res.*, 32:113–140, 2002.
- [13] L. C. Evans, H. M. Soner, and P. E. Souganidis. Phase transitions and generalized motion by mean curvature. *Comm. Pure Appl. Math.*, 45(9):1097–1123, 1992.
- [14] Y. G. Chen, Y. Giga, and S. Goto. Uniqueness and existence of viscosity solutions of generalized mean curvature flow equations. *Proc. Japan Acad. Ser. A Math. Sci.*, 65(7):207–210, 1989.
- [15] L. C. Evans and J. Spruck. Motion of level sets by mean curvature. I. *J. Differential Geom.*, 33(3):635–681, 1991.
- [16] T. Ilmanen. Convergence of the Allen-Cahn equation to Brakke’s motion by mean curvature. *J. Differential Geom.*, 38(2):417–461, 1993.
- [17] F. Liu and J. Shen. Stabilized semi-implicit spectral deferred correction methods for Allen-Cahn and Cahn-Hilliard equations. *Math. Methods Appl. Sci.*, 38:4564–4575, 2013.
- [18] X. Feng and Y. Li. Analysis of symmetric interior penalty discontinuous Galerkin methods for the Allen-Cahn equation and the mean curvature flow. *IMA J. Numer. Anal.*, 35(4):1622–1651, 2015.
- [19] B. Karasözen, M. Uzunca, A. S. Filibelioglu, and H. Yücel. Energy stable discontinuous Galerkin finite element method for the Allen-Cahn equation. *Int. J. Comput. Methods*, 13(3):1850013, 2018.
- [20] J. Shen and X. Yang. Numerical approximations of Allen-Cahn and Cahn-Hilliard equations. *Discret. Contin. Dyn.-A*, 28:1669–1691, 2010.
- [21] X. Feng, H. Song, T. Tang, and J. Yang. Nonlinear stability of the implicit-explicit methods for the Allen-Cahn equation. *Inverse Probl. Imag.*, 7:679–695, 2013.
- [22] E. Celledoni, V. Grimm, R. I. McLachlan, D. I. McLaren, D. O’Neale, B. Owren, and G. R. W. Quispel. Preserving energy resp. dissipation in numerical PDEs using the "Average Vector Field" method. *J. Comput. Phys.*, 231:6770–6789, 2012.
- [23] J. Shen, C. Wang, X. Wang, and S. Wise. Second-order convex splitting schemes for gradient flows with Enhrich-Schwoebel type energy: Application to thin film epitaxy. *SIAM. J. Numer. Anal.*, 50:105–125, 2012.
- [24] T. K. Akinfe and A. C. Loyinmi. An improved differential transform scheme implementation on the generalized Allen-Cahn equation governing oil pollution dynamics in oceanography. *Partial Differ. Equ. Appl. Math.*, 6:100416, 2022.
- [25] S. Hussain, F. Haq, A. Shah, D. Abduvalieva, and A. Shokri. Comparison of approximate analytical and numerical solutions of the Allen Cahn equation. *Int. J. Differ. Equ.*, 2024(1):8835138, 2024.
- [26] A. Krizhevsky, I. Sutskever, and G. Hinton. Imagenet classification with deep convolutional neural networks. In F. Pereira, C. J. C. Burges, L. Bottou, and K. Q. Weinberger, editors, *Advances in Neural Information Processing Systems* 25, pages 1097–1105. Curran Associates, Inc., 2012.
- [27] B. M. Lake, R. Salakhutdinov, and J. B. Tenenbaum. Human-level concept learning through probabilistic program induction. *Science*, 350:1332–1338, 2015.
- [28] J. Berg and K. Nystrom. A unified deep artificial neural network approach to partial differential equations in complex geometries. *Neurocomputing*, 317:28–41, 2018.
- [29] W. E and B. Yu. The deep Ritz method: A deep learning-based numerical algorithm for solving variational problems. *Commun. Math. Stat.*, 6:1–12, 2018.
- [30] B. Li, S. Tang, and H. Yu. Better approximations of high dimensional smooth functions by deep neural networks with rectified power units. *Commun. Comput. Phys.*, 27:379–411, 2020.
- [31] L. Lu, X. Meng, Z. Mao, and G. E. Karniadakis. DeepXDE: A deep learning library for solving differential equations. *SIAM Rev.*, 63(1):208–228, 2021.
- [32] M. Raissi, P. Perdikaris, and G. E. Karniadakis. Physics-informed neural networks: A deep learning framework for solving forward and inverse problems involving nonlinear partial differential equations. *J. Comput. Phys.*, 378:689–707, 2019.

- [33] J. Sirignano and K. Spiliopoulos. DGM: A deep learning algorithm for solving partial differential equations. *J. Comput. Phys.*, 375:1339–1364, 2018.
- [34] Y. Liao and P. Ming. Deep Nitsche method: Deep Ritz method with essential boundary conditions. *Commun. Comput. Phys.*, 29:1365–1384, 2021.
- [35] G. Cybenko. Approximation by superpositions of a sigmoidal function. *Math. Control Signals Systems*, 2(4):303–314, 1989.
- [36] K. Hornik, M. Stinchcombe, and H. White. Multilayer feedforward networks are universal approximators. *Neural Netw.*, 2(5):359–366, 1989.
- [37] Y. Chen, L. Lu, G. E. Karniadakis, and L. D. Negro. Physics-informed neural networks for inverse problems in nano-optics and metamaterials. *Opt. Express*, 28(8):11618, 2020.
- [38] Z. Mao, A. D. Jagtap, and G. E. Karniadakis. Physics-informed neural networks for high-speed flows. *Comput. Methods Appl. Mech. Engrg.*, 360:112789, 2020.
- [39] M. Sikora, P. Krukowski, A. Paszyńska, and M. Paszyński. Comparison of physics informed neural networks and finite element method solvers for advection–dominated diffusion problems. *J. Comput. Sci.*, 81:102340, 2024.
- [40] M. Daneker, Z. Zhang, G. E. Karniadakis, and L. Lu. *Systems Biology: Identifiability Analysis and Parameter Identification via Systems-Biology-Informed Neural Networks*, pages 87–105. Springer US, New York, NY, 2023.
- [41] L. Lu, R. Pestourie, W. Yao, Z. Wang, F. Verdugo, and S. G. Johnson. Physics-informed neural networks with hard constraints for inverse design. *SIAM J. Sci. Comput.*, 43(6):B1105–B1132, 2021.
- [42] G. Pang, L. Lu, and G. E. Karniadakis. fPINNs: Fractional physics-informed neural networks. *SIAM J. Sci. Comput.*, 41(4):A2603–A2626, 2019.
- [43] D. Zhang, L. Guo, and G. E. Karniadakis. Quantifying total uncertainty in physics-informed neural networks for solving forward and inverse stochastic problems. *J. Comput. Phys.*, 397:108850, 2019.
- [44] S. Karumuri, R. Tripathy, I. Bilonis, and J. Panchal. Simulator-free solution of high-dimensional stochastic elliptic partial differential equations using deep neural networks. *J. Comput. Phys.*, 404:109120, 2020.
- [45] A. F. Psaros, K. Kawaguchi, and G. E. Karniadakis. Meta-learning PINN loss functions. *J. Comput. Phys.*, 458:111121, 2022.
- [46] J. Yu, L. Lu, X. Meng, and G. E. Karniadakis. Gradient-enhanced physics informed neural networks for forward and inverse PDE problems. *Comput. Methods Appl. Mech. Eng.*, 93:114823, 2022.
- [47] S. Wang, Y. Teng, and P. Perdikaris. Understanding and mitigating gradient flow pathologies in physics-informed neural networks. *SIAM J. Sci. Comput.*, 43(5):A3055–A3081, 2021.
- [48] A. D. Jagtap and G. E. Karniadakis. Extended physics-informed neural networks (XPINNs): A generalized space-time domain decomposition based deep learning framework for nonlinear partial differential equations. *Commun. Comput. Phys.*, 28(5):2002–2041, 2020.
- [49] C. Wu, M. Zhu, Q. Tan, Y. Kartha, and L. Lu. A comprehensive study of non-adaptive and residual-based adaptive sampling for physics-informed neural networks. *Comput. Methods Appl. Mech. Eng.*, 403:115671, 2023.
- [50] C. L. Wight and J. Zhao. Solving Allen–Cahn and Cahn–Hilliard equations using the adaptive physics informed neural networks. *Commun. Comput. Phys.*, 29:930–954, 2021.
- [51] S. Wang, S. Sankaran, and P. Perdikaris. Respecting causality for training physics-informed neural networks. *Comput. Methods Appl. Mech. Eng.*, 421:116813, 2024.
- [52] A. D. Jagtap, K. Kawaguchi, and G. E. Karniadakis. Adaptive activation functions accelerate convergence in deep and physics-informed neural networks. *J. Comput. Phys.*, 404:109136, 2020.
- [53] S. Dong and N. Ni. A method for representing periodic functions and enforcing exactly periodic boundary conditions with deep neural networks. *J. Comput. Phys.*, 435:110242, 2021.
- [54] Y. Shin, J. Darbon, and G. E. Karniadakis. On the convergence of physics informed neural networks for linear second-order elliptic and parabolic type PDEs. *Commun. Comput. Phys.*, 28(5):2042–2074, 2020.
- [55] S. Mishra and R. Molinaro. Estimates on the generalization error of physics-informed neural networks for approximating a class of inverse problems for PDEs. *IMA J. Numer. Anal.*, 42(2):981–1022, 2021.
- [56] S. Mishra and R. Molinaro. Estimates on the generalization error of physics-informed neural networks for approximating PDEs. *IMA J. Numer. Anal.*, 43(1):1–43, 2022.
- [57] T. De Ryck, A. D. Jagtap, and S. Mishra. Error estimates for physics-informed neural networks approximating the Navier–Stokes equations. *IMA J. Numer. Anal.*, 44(1):83–119, 2023.

- [58] Y. Jiao, Y. Lai, D. Li, X. Lu, F. Wang, Y. Wang, and J. Z. Yang. A rate of convergence of physics informed neural networks for the linear second order elliptic PDEs. *Commun. Comput. Phys.*, 31(4):1272–1295, 2022.
- [59] G. Zhang, J. Lin, Q. Zhai, H. Yang, X. Chen, X. Zheng, and I. T. Leong. A priori error estimation of physics-informed neural networks solving Allen–Cahn and Cahn–Hilliard equations, 2024.
- [60] Y. Qian, Y. Zhang, Y. Huang, and S. Dong. Physics-informed neural networks for approximating dynamic (hyperbolic) PDEs of second order in time: Error analysis and algorithms. *J. Comput. Phys.*, 495:112527, 2023.
- [61] T. Poggio, H. Mhaskar, L. Rosasco, B. Miranda, and Q. Liao. Why and when can deep-but not shallow-networks avoid the curse of dimensionality: A review. *Int. J. Autom. Comput.*, 14:503–519, 2017.
- [62] T. G. Grossmann, U. J. Komorowska, J. Latz, and C.-B. Schönlieb. Can physics-informed neural networks beat the finite element method? *IMA J. Appl. Math.*, 89(1):143–174, 2024.
- [63] Y. Geng, Y. Teng, Z. Wang, and L. Ju. A deep learning method for the dynamics of classic and conservative Allen-Cahn equations based on fully-discrete operators. *J. Comput. Phys.*, 496:112589, 2024.
- [64] H. Xu, J. Chen, and F. Ma. Adaptive deep learning approximation for Allen-Cahn equation. In D. Groen, C. de Mulatier, M. Paszynski, V. V. Krzhizhanovskaya, J. J. Dongarra, and P. M. A. Sloot, editors, *Computational Science – ICCS 2022*, pages 271–283, Cham, 2022. Springer International Publishing.
- [65] R. Matthey and S. Ghosh. A novel sequential method to train physics informed neural networks for Allen Cahn and Cahn Hilliard equations. *Comput. Methods Appl. Mech. Eng.*, 390:114474, 2022.
- [66] A. Singh and R. K. Sinha. Multioutput FOSLS deep neural network for solving Allen–Cahn equation. *Math. Models Comput. Simul.*, 15:1132–1146, 2023.
- [67] J. Guo, H. Wang, and C. Hou. An adaptive energy-based sequential method for training PINNs to solve gradient flow equations. *Appl. Math. Comput.*, 479:128890, 2024.
- [68] G.-Z. Wu, Y. Fang, N. A. Kudryashov, Y.-Y. Wang, and C.-Q. Dai. Prediction of optical solitons using an improved physics-informed neural network method with the conservation law constraint. *Chaos Soliton Fract.*, 159:112143, 2022.
- [69] S. Lin and Y. Chen. A two-stage physics-informed neural network method based on conserved quantities and applications in localized wave solutions. *J. Comput. Phys.*, 457:111053, 2022.
- [70] I. Goodfellow, Y. Bengio, and A. Courville. Deep feedforward networks. In *Deep Learning*, pages 174–197. MIT Press, 2017.
- [71] T. Szandała. *Review and Comparison of Commonly Used Activation Functions for Deep Neural Networks*, pages 203–224. Springer Singapore, Singapore, 2021.
- [72] X. Glorot and Y. Bengio. Understanding the difficulty of training deep feedforward neural networks. *J. Mach. Learn. Res.*, 9:249–256, 2010.
- [73] K. M. He, X. Y. Zhang, S. Q. Ren, and J. Sun. Delving deep into rectifiers: Surpassing human-level performance on imagenet classification. In *Proceedings of the IEEE International Conference on Computer Vision (ICCV)*, pages 1026–1034, 2015.
- [74] A. G. Baydin, B. A. Pearlmutter, A. A. Radul, and J. M. Siskind. Automatic differentiation in machine learning: A survey. *J. Mach. Learn. Res.*, 18:1–43, 2018.
- [75] M. D. Shields and J. Zhang. The generalization of Latin hypercube sampling. *Reliab. Eng. Syst. Saf.*, 148:96–108, 2016.
- [76] M. Renardy, L. R. Joslyn, J. A. Millar, and D. E. Kirschner. To Sobol or not to Sobol? The effects of sampling schemes in systems biology applications. *Math. Biosci.*, 337:108593, 2021.
- [77] J. M. Hanna, J. V. Aguadoa, S. Comas-Cardona, R. Askri, and D. Borzacchielloa. Residual-based adaptivity for two-phase flow simulation in porous media using Physics-informed Neural Networks. *Comput. Methods Appl. Mech. Engrg.*, 396:115100, 2022.
- [78] L. Bottou, F. E. Curtis, and J. Nocedal. Optimization methods for large-scale machine learning. *SIAM Rev.*, 60(2):223–311, 2018.
- [79] J. Nocedal and S. J. Wright. *Numerical Optimization*. Springer Verlag, Berlin, Heidelberg, New York, second edition, 2006.
- [80] W. Dörfler. A convergent adaptive algorithm for Poisson’s equation. *SIAM J. Numer. Anal.*, 33:1106–1124, 1996.
- [81] T. Akiba, S. Sano, T. Yanase, T. Ohta, and M. Koyama. Optuna: A next-generation hyperparameter optimization framework. In *Proceedings of the 25th ACM SIGKDD International Conference on Knowledge Discovery and Data Mining*, 2019.

- [82] P. Ren, C. Rao, Y. Liu, J.-X. Wang, and H. Sun. Phycrnet: Physics-informed convolutional-recurrent network for solving spatiotemporal PDEs. *Comput. Methods Appl. Math.*, 389:114399, 2022.
- [83] Y. Wang, X. Han, C.-Y. Chang, D. Zha, U. Braga-Neto, and X. Hu. Auto-PINN: Understanding and optimizing physics-informed neural architecture, 2023.
- [84] P. Pantidis, H. Eldababy, C. M. Tagle, and M. E. Mobasher. Error convergence and engineering-guided hyperparameter search of PINNs: Towards optimized I-FENN performance. *Comput. Methods Appl. Math.*, 414:116160, 2023.
- [85] N. Hasebrook, F. Morsbach, N. Kannengießer, M. Zöller, J. Franke, M. Lindauer, F. Hutter, and A. Sunyaev. Practitioner motives to select hyperparameter optimization methods, 2023.
- [86] K. He, X. Zhang, S. Ren, and J. Sun. Deep residual learning for image recognition. pages 770–778, Las Vegas, NV, 2016. 2016 IEEE Conference on Computer Vision and Pattern Recognition (CVPR), IEEE.
- [87] D. P. Kingma and J. Ba. Adam: A method for stochastic optimization, 2017.
- [88] T. A. Driscoll, N. Hale, and L. N. Trefethen. *Chebfun Guide*. Pafnuty Publications, Oxford, 2014.
- [89] S. J. Pan and Q. Yang. A survey on transfer learning. *IEEE Trans. Knowl. Data Eng.*, 22(10):1345–1359, 2010.
- [90] Y. Li, H. G. Lee, D. Jeong, and J. Kim. An unconditionally stable hybrid numerical method for solving the Allen-Cahn equation. *Comput. Math. Appl.*, 60:1591–1606, 2010.
- [91] D. Li, C. Quan, and J. Xu. Stability and convergence of Strang splitting. Part I: Scalar Allen-Cahn equation. *J. Comput. Phys.*, 458:111087, 2022.
- [92] J. Shen, T. Tang, and J. Yang. On the maximum principle preserving schemes for the generalized Allen–Cahn equation. *Commun. Math. Sci.*, 14(6):1517–1534, 2016.
- [93] S. Filip, A. Javeed, and L. N. Trefethen. Smooth random functions, random ODEs, and Gaussian processes. *SIAM Rev.*, 61:185–205, 2019.
- [94] R. Li, Y. Gao, and Z. Chen. Adaptive discontinuous Galerkin finite element methods for the Allen–Cahn equation on polygonal meshes. *Numer. Algorithms*, 95:1981–2014, 2024.
- [95] Y. Wang, X. Xiao, and X. Feng. Efficient numerical simulation of the conserved Allen–Cahn type flow-coupled binary fluid-surfactant model by a dimension splitting method. *Int. J. Multiph. Flow*, 169:104607, 2023.